Spatiotemporal control of light by Bloch-mode dispersion in multi-core fibers

Per Dalgaard Rasmussen[1,2], Andrey A. Sukhorukov[1], Dragomir N. Neshev[1], Wiesław Krolikowski[1], Ole Bang[2], Jesper Lægsgaard[2], and Yuri S. Kivshar[1]

[1]*Nonlinear Physics Centre and Laser Physics Centre, Centre for Ultrahigh bandwidth Devices for Optical Systems (CUDOS), Research School of Physical Sciences and Engineering, Australian National University, Canberra, ACT 0200, Australia*
[2]*DTU Fotonik, Department of Photonics Engineering, Technical University of Denmark, Ørsteds Plads 345V, DK-2800 Kgs. Lyngby, Denmark*

pdr@com.dtu.dk

Abstract: We study theoretically the dispersion properties of Bloch modes and nonlinearly-induced defect states in two-dimensional waveguide arrays. We define the conditions for achieving anomalous group-velocity dispersion and discuss possibilities for generation of spatiotemporal solitons.

© 2008 Optical Society of America

OCIS codes: (230.7370) Waveguides; (190.5530) Pulse propagation and solitons

References and links

1. Yu. S. Kivshar and G. P. Agrawal, *Optical Solitons: From Fibers to Photonic Crystals* (Academic Press, San Diego, 2003).
2. G. I. Stegeman and M. Segev, "Optical spatial solitons and their interactions: Universality and diversity," Science **286,** 1518–1523 (1999).
3. G. P. Agrawal, *Nonlinear Fiber Optics*, fourth ed. (Academic Press, New York, 2007).
4. Y. Silberg, "Collapse of optical pulses," Opt. Lett. **15,** 1282–1284 (1990).
5. A. B. Blagoeva, S. G. Dinev, A. A. Dreischuh, and A. Naidenov, "Light bullets formation in a bulk media," IEEE J. Quantum Electron. **QE-27**, 2060 (1991).
6. F. Wise and P. Di Trapani, "The hunt for light bullets - spatiotemporal solitons," Opt. Photon. News **13,** 28–32 (2002).
7. B. A. Malomed, D. Mihalache, F. Wise, and L. Torner, "Spatiotemporal optical solitons," J. Opt. B: Quantum Semicl. Opt. **7,** R53–R72 (2005).
8. H. S. Eisenberg, R. Morandotti, Y. Silberberg, S. Bar Ad, D. Ross, and J. S. Aitchison, "Kerr spatiotemporal self-focusing in a planar glass waveguide," Phys. Rev. Lett. **87,** 043902–4 (2001).
9. D. Cheskis, S. Bar Ad, R. Morandotti, J. S. Aitchison, H. S. Eisenberg, Y. Silberberg, and D. Ross, "Strong spatiotemporal localization in a silica nonlinear waveguide array," Phys. Rev. Lett. **91,** 223901–4 (2003).
10. N. I. Nikolov, D. Neshev, O. Bang, and W. Z. Krolikowski, "Quadratic solitons as nonlocal solitons," Phys. Rev. E **68,** 036614–5 (2003).
11. X. Liu, L. J. Qian, and F. W. Wise, "Generation of optical spatiotemporal solitons," Phys. Rev. Lett. **82,** 4631–4634 (1999).
12. X. Liu, K. Beckwitt, and F. Wise, "Two-dimensional optical spatiotemporal solitons in quadratic media," Phys. Rev. E **62,** 1328–1340 (2000).
13. A. B. Aceves, C. De Angelis, A. M. Rubenchik, and S. K. Turitsyn, "Multidimensional solitons in fiber arrays," Opt. Lett. **19,** 329–331 (1994).
14. E. W. Laedke, K. H. Spatschek, and S. K. Turitsyn, "Stability of discrete solitons and quasicollapse to intrinsically localized modes," Phys. Rev. Lett. **73,** 1055–1059 (1994).
15. A. B. Aceves, G. G. Luther, C. De Angelis, A. M. Rubenchik, and S. K. Turitsyn, "Energy localization in nonlinear fiber arrays - collapse-effect compressor," Phys. Rev. Lett. **75,** 73–76 (1995).

16. A. B. Aceves, M. Santagiustina, and C. De Angelis, "Analytical study of nonlinear-optical pulse dynamics in arrays of linearly coupled waveguides," J. Opt. Soc. Am. B **14,** 1807–1815 (1997).
17. D. Mihalache, D. Mazilu, F. Lederer, and Yu. S. Kivshar, "Stable discrete surface light bullets," Opt. Express **15,** 589–595 (2007), http://www.opticsinfobase.org/abstract.cfm?URI=oe-15-2-589 .
18. D. N. Christodoulides, F. Lederer, and Y. Silberberg, "Discretizing light behaviour in linear and nonlinear waveguide lattices," Nature **424,** 817–823 (2003).
19. D. N. Christodoulides and R. I. Joseph, "Discrete self-focusing in nonlinear arrays of coupled wave-guides," Opt. Lett. **13,** 794–796 (1988).
20. H. S. Eisenberg, Y. Silberberg, R. Morandotti, A. R. Boyd, and J. S. Aitchison, "Discrete spatial optical solitons in waveguide arrays," Phys. Rev. Lett. **81,** 3383–3386 (1998).
21. J. W. Fleischer, T. Carmon, M. Segev, N. K. Efremidis, and D. N. Christodoulides, "Observation of discrete solitons in optically induced real time waveguide arrays," Phys. Rev. Lett. **90,** 023902–4 (2003).
22. D. Neshev, E. Ostrovskaya, Y. Kivshar, and W. Krolikowski, "Spatial solitons in optically induced gratings," Opt. Lett. **28,** 710–712 (2003).
23. F. Chen, M. Stepić, C. Rüter, D. Runde, D. Kip, V. Shandarov, O. Manela, and M. Segev, "Discrete diffraction and spatial gap solitons in photovoltaic LiNbO3 waveguide arrays," Opt. Express **13,** 4314–4324 (2005), http://www.opticsinfobase.org/abstract.cfm?URI=oe-13-11-4314 .
24. A. Fratalocchi, G. Assanto, K. A. Brzdakiewicz, and M. A. Karpierz, "Discrete propagation and spatial solitons in nematic liquid crystals," Opt. Lett. **29,** 1530–1532 (2004).
25. J. W. Fleischer, M. Segev, N. K. Efremidis, and D. N. Christodoulides, "Observation of two-dimensional discrete solitons in optically induced nonlinear photonic lattices," Nature **422,** 147–150 (2003).
26. C. R. Rosberg, D. N. Neshev, A. A. Sukhorukov, W. Krolikowski, and Yu. S. Kivshar, "Observation of nonlinear self-trapping in triangular photonic lattices," Opt. Lett. **32,** 397–399 (2007).
27. A. Szameit, D. Blömer, J. Burghoff, T. Schreiber, T. Pertsch, S. Nolte, A. Tünnermann, and F. Lederer, "Discrete nonlinear localization in femtosecond laser written waveguides in fused silica," Opt. Express **13,** 10552–10557 (2005), http://www.opticsinfobase.org/abstract.cfm?URI=oe-13-26-10552 .
28. F. Couny, F. Benabid, P. J. Roberts, M. T. Burnett, and S. A. Maier, "Identification of Bloch-modes in hollow-core photonic crystal fiber cladding," Opt. Express **15,** 325–338 (2007), http://www.opticsinfobase.org/abstract.cfm?URI=oe-15-2-325 .
29. C. R. Rosberg, F. H. Bennet, D. N. Neshev, P. D. Rasmussen, O. Bang, W. Krolikowski, A. Bjarklev, and Yu. S. Kivshar, "Tunable diffraction and self-defocusing in liquid-filled photonic crystal fibers," Opt. Express **15,** 12145–12150 (2007), http://www.opticsinfobase.org/abstract.cfm?URI=oe-15-19-12145 .
30. J. Jasapara, T. H. Her, R. Bise, R. Windeler, and D. J. DiGiovanni, "Group-velocity dispersion measurements in a photonic bandgap fiber," J. Opt. Soc. Am. B **20,** 1611–1615 (2003).
31. P. Mach, M. Dolinski, K. W. Baldwin, J. A. Rogers, C. Kerbage, R. S. Windeler, and B. J. Eggleton, "Tunable microfluidic optical fiber," Appl. Phys. Lett. **80,** 4294–4296 (2002).
32. F. Luan, A. K. George, T. D. Hedley, G. J. Pearce, D. M. Bird, J. C. Knight, and P. St. Russell, "All-solid photonic bandgap fiber," Opt. Lett. **29,** 2369–2371 (2004).
33. T. Pertsch, U. Peschel, J. Kobelke, K. Schuster, H. Bartelt, S. Nolte, A. Tünnermann, and F. Lederer, "Nonlinearity and disorder in fiber arrays," Phys. Rev. Lett. **93,** 053901–4 (2004).
34. U. Röpke, H. Bartelt, S. Unger, K. Schuster, and J. Kobelke, "Two-dimensional high-precision fiber waveguide arrays for coherent light propagation," Opt. Express **15,** 6894–6899 (2007), http://www.opticsinfobase.org/abstract.cfm?URI=oe-15-11-6894 .
35. S. G. Johnson and J. D. Joannopoulos, "Block-iterative frequency-domain methods for Maxwell's equations in a planewave basis," Opt. Express **8,** 173–190 (2001), http://www.opticsinfobase.org/abstract.cfm?URI=oe-8-3-173 .
36. A. Samoc, "Dispersion of refractive properties of solvents: chloroform, toluene, benzene, and carbon disulfide in ultraviolet, visible, and near-infrared," J. Appl. Phys. **94,** 6167–6174 (2003).
37. D. N. Nikogosyan, *Properties of Optical and Laser-Related Materials: A Handbook* (Wiley, Chichester, UK, 1997).
38. K. Okamoto, *Fundamentals of optical waveguides* (Academic Press, San Diego, 2000).
39. I. P. Nikolakakos, A. Major, J. S. Aitchison, and P. W. E. Smith, "Broadband characterization of the nonlinear optical properties of common reference materials," IEEE J. Sel. Top. Quantum Electron. **10,** 1164–1170 (2004).
40. COMSOL Multiphysics 3.3 (2007), COMSOL Inc. (http://www.comsol.com/).
41. P. G. Kevrekidis, B. A. Malomed, and Y. B. Gaididei, "Solitons in triangular and honeycomb dynamical lattices with the cubic nonlinearity," Phys. Rev. E **66,** 016609–10 (2002).

1. Introduction

A general property of the evolution of an optical wavepacket is its natural spreading in space and time. This is due to the fact that the various spatial and spectral components of the wave

propagate under slightly different directions and with different velocity in a material. These effects are well known as beam diffraction and group-velocity dispersion (GVD). Examples are laser beam spreading in bulk media and pulse broadening in optical fibres. An important way to counteract these two effects is provided by the material nonlinearity. At high laser powers the nonlinearity-induced refractive index change in the material can provide a confining potential for the wavepacket, thus keeping it together without spreading. This wave confinement is associated with the formation of an optical soliton. The nonlinear localization in space and in time are usually considered independently in the form of spatial or temporal solitons [1]. Spatial solitons form when the natural beam diffraction is compensated by *positive self-focusing nonlinearity* [2]. Similarly, when the positive material nonlinearity is compensated by the anomalous pulse dispersion temporal solitons can be formed [3].

One might think that simple combination of spatial and temporal localization will give rise to a new entity localized in three-dimensions (3D) (one time and two spatial dimensions) called *spatiotemporal soliton* (STS) or "light bullets" [4–7]. Generally, STSs can not be factored into separate spatial and temporal dependencies, simply because both the spatial and temporal dispersive properties are coupled through the same material nonlinearity. Therefore, the formation of STSs can only be realized when the characteristic diffraction and dispersion lengths are equalized [7]. This condition imposes requirements for long propagation distances or high-energy (μJ) ultra-short (femtosecond) pulses. However, even when this necessary condition can be satisfied, it might not be sufficient. In a Kerr-type nonlinear medium, 3D STSs suffer collapse when the input power is above a critical value [4]. Therefore, the experimental observation of STS requires special methods or materials for suppression of the wave collapse. Commonly used techniques employ multi-photon absorption and stimulated Raman scattering [8,9]. Such processes appear naturally when high intensity pulses are used, however, due to their dissipative nature, the resulting pulses loose energy during propagation and spread in time and space. Nonparaxiality, higher-order dispersion, or nonlocal nonlinearities can also counteract the collapse. The latter one appeared especially promising for experimental realization, as cascaded quadratic nonlinearity naturally gives rise to effectively nonlocal nonlinear response [10]. Indeed, quadratic type of interaction allowed for the successful demonstration of STS in 2D (time and one spatial coordinate) [11,12], however the nature of these experiments does not allow for realization of truly 3D STS.

The search for alternative and practically feasible methods for realizing STS puts forward the idea of multidimensional solitons in fibre arrays or multi-core fibres. Actively studied in 2D geometry (time plus one spatial dimension) such discrete systems enable arrest of the collapse even with Kerr-type nonlinearity, and allow for a trivial extension into two transverse spatial dimensions [13–16]. However, the development of the discreteness in a practical system suitable for experimental testing remains unexplored. In this work we present a novel platform for realization of stable 3D light bullets based on liquid-infiltrated cladding of a photonic crystal fibre (PCF). The suggested platform offers the advantages of high-quality commercially fabricated structures, long propagation distances in a fiber geometry, dispersion and diffraction engineering by selection and excitation of Bloch modes of the system, as well as suppression of wave collapse due to discreetness. Additionally, the use of liquid infiltration offers strong nonlinear response (up to 1000 times higher than silica glass), which allows for the use of low-power lasers. Finally, such periodic structures have a finite transverse extent and offer the possibility for exploration of spatiotemporal nonlinear surface states [17].

2. Bandgap structure of infiltrated photonic-crystal fibers

In recent years new fabrication techniques have boosted research of nonlinear waveguide arrays [18]. Spatial localization in 1D waveguide arrays suggested almost 20 years ago [19]

was realized experimentally in semiconductor materials [20], photorefractive optical lattices [21–23], and liquid crystal waveguide arrays [24]. The extension of this discrete light localisation in higher dimensions lead to the observation of 2D discrete solitons in square [25] and hexagonal [26] optically induced photonic lattices, as well as in laser written waveguide arrays in fused silica [27]. In all these works however, only spatial nonlinear effects have been explored. On the other hand PCFs are the system of choice for manipulation of temporal dispersion of pulses confined in a prefabricated defect in the center of a periodic structure. The extended cladding region of such fibers, however, offers a new opportunity to combine the temporal dispersion management with spatial effects through excitation of Bloch modes. Selective excitation of cladding Bloch modes has been indeed recently demonstrated [28], and nonlinear spatial control in infiltrated PCFs was proven to be experimentally feasible [29].

However, the combination of spatial and temporal nonlinear control of optical wave packets in the extended cladding region of PCFs remains unexplored. To study their spatiotemporal nonlinear dynamics we model the extended cladding region of a PCF infiltrated with a high-refractive index liquid as a perfect 2D waveguide array and consider its bandgap structure. We study a hexagonal arrangement of high index rods in a silica background as the one showed in Fig. 1(a,b). Such a structure is known to possess bandgaps for out-of-plane propagation, and it can be realized in two ways: either by infiltrating the air-holes of a standard photonic crystal fiber with a high-index fluid [29–31] as mentioned above, or by using the stack and draw technique with glass rods having different refractive indices [32–34].

The eigenmodes of 2D periodic structures are obtained by solving Maxwell's equations, which in the case where there are no free currents and charges, reduce to the wave equation

$$\nabla \times \frac{1}{\varepsilon(\mathbf{r})} \nabla \times \mathbf{H}_\omega(\mathbf{r}) = \frac{\omega^2}{c^2} \mathbf{H}_\omega(\mathbf{r}),\tag{1}$$

where $\varepsilon(\mathbf{r})$ is the periodic dielectric function, and c is the speed of light in vacuum. ω is the angular frequency, and a harmonic time dependence of the magnetic field has been assumed, i.e. $\mathbf{H}(\mathbf{r},t) = \mathbf{H}_\omega(\mathbf{r})\exp(-i\omega t)$. Since the considered structure is perfectly periodic (no defects), one can use Bloch's Theorem to calculate the modes

$$\mathbf{H}_{\mathbf{k}_\perp,\beta,m}(\mathbf{r},t) = \mathbf{u}_{\mathbf{k}_\perp,m}(\mathbf{r}_\perp)\exp[i(\mathbf{k}_\perp \cdot \mathbf{r}_\perp + \beta z - \omega_m(\mathbf{k}_\perp,\beta)t)],\tag{2}$$

where the functions $\mathbf{u}_{\mathbf{k}_\perp,m}(\mathbf{r}_\perp)$ are periodic, with the same period as $\varepsilon(\mathbf{r})$. β is the z-component of the wavevector, while the transverse part of the wavevector is given by $\mathbf{k}_\perp$. The index m in Eq. (2) denotes the eigenvalue number, where the smallest eigenvalue is $m = 1$.

For the numerical solution of Eq. (1) we use a fully-vectorial plane-wave method [35]. For in-plane propagation ($\beta = 0$) there are no bandgaps in the structure, but for out-of-plane propagation bandgaps begin to appear as β increases. In Fig. 1(c) the regions with a photonic bandgap are shown for a fiber with $d/\Lambda = 0.50$, where d is the hole diameter, and Λ is the pitch (interhole distance). The refractive index of the background material is fixed at 1.44 (corresponding to silica at the wavelength of 1.5 m), and the refractive index inside the holes is 1.59 corresponding to the refractive index of CS_2 at a wavelength of 1.5 m [36]. We see that a bandgap opens up when $\lambda/\Lambda < 1.15$. The individual waveguides are single-mode as long as the V-parameter [$V = \pi d(n_{co}^2 - n_{cl}^2)^{1/2}/\lambda$] is less than 2.405. This cutoff is indicated in Fig. 1(c) with a vertical line at $\lambda/\Lambda = 0.44$. The dispersion of the lowest lying bands is shown in Fig. 1(d) for a normalized wavelength of $\lambda/\Lambda = 0.5$. The fundamental band ($m = 1$) is doubly degenerate, which is analogous to the two polarizations of the fundamental HE_{11}-mode of an individual high-index rod (step index fiber). The second band is nearly degenerate for long wavelengths, but as the wavelength decreases a polarization splitting appears.
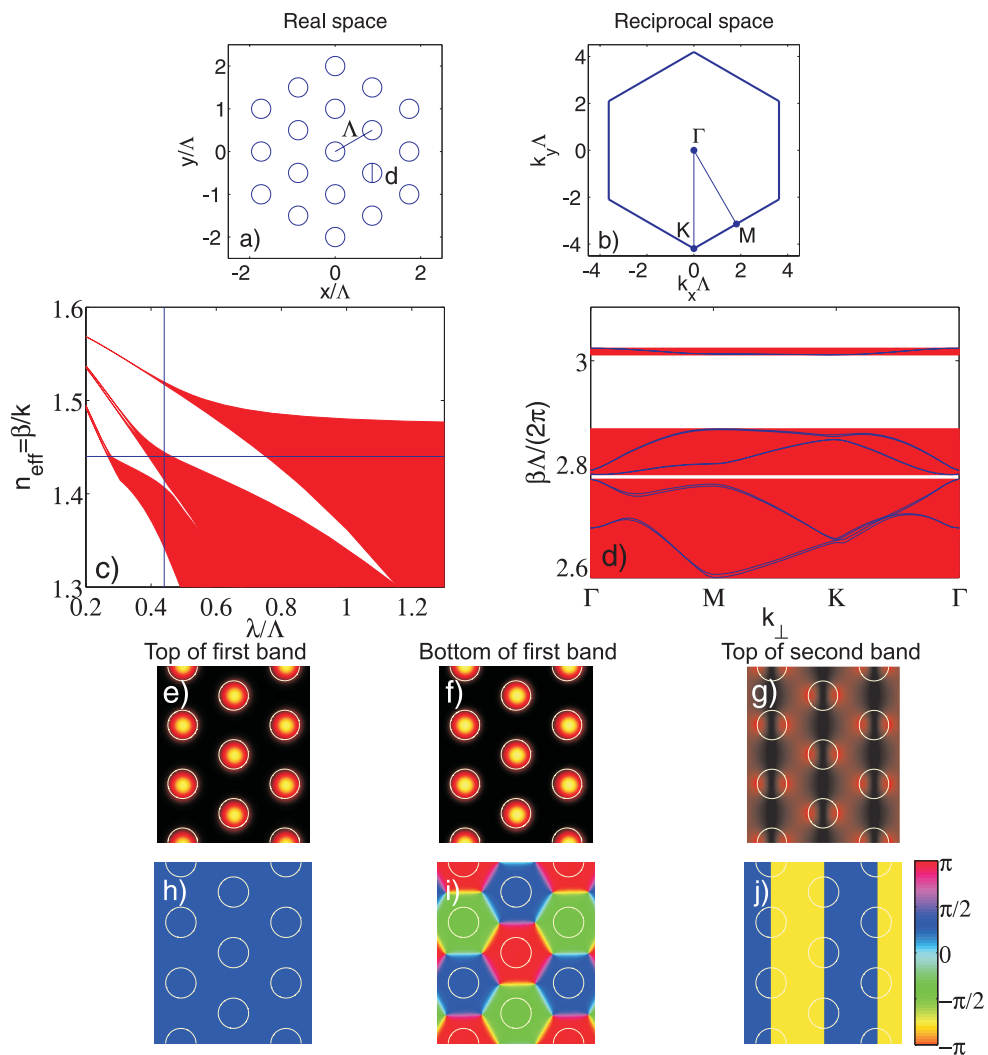
Fig. 1. (a) Real space hexagonal lattice and (b) the corresponding reciprocal space lattice. The triangle ΓMK defines the irreducible Brillouin zone. (c) Allowed modes in an array with $d/\Lambda = 0.5$. The refractive index inside the holes is 1.59, and the refractive index of the background material is 1.44. The shaded areas indicate bands where modes are allowed, and the horizontal line indicates the refractive index of the solid material. The vertical line marks where an individual capillary becomes single-mode. (d) Photonic band structure for a constant normalized wavelength of $\lambda/\Lambda = 0.5$ and $d/\Lambda = 0.5$. (e)-(g) Intensities of the E-fields corresponding to the modes at the top and bottom of the first band and the top of the second band also for a normalized wavelength of $\lambda/\Lambda = 0.5$. The corresponding phases are shown in (h)-(i).

In Figs. 1(e)-(j) we plot the intensities and phases of the strongest components of the E-fields of the modes for $\lambda/\Lambda = 0.5$. We see that the top of the first band (Γ-point) has LP_{01}-like solutions with maximum intensity located inside the high index holes and a flat phase structure. The bottom of the first band (K-point) has a similar intensity distribution as the top of the first band, but the phase varies by $\pm 2\pi/3$ between adjacent holes. The mode at the top of the second band corresponds either to the mode at the M-point for long wavelengths, or to the mode at the K-point for short wavelengths. For the specific structure considered in Fig. 1 this cross-over happens close to $\lambda/\Lambda \approx 0.33$, as for $\lambda/\Lambda > 0.33$ the top of the second band occurs at the M-point, while for $\lambda/\Lambda < 0.33$ the top of the second band occurs at the K-point. The modes in the second band have LP_{11}-like intensity patterns, i.e. they resemble dipoles, with two maxima inside each high-index region. The phases are staggered in the vertical direction, and have π-phase jumps that go through the center of each high-index region. Notice that the fields and phases for the first band are plotted for only the strongest component of the electric field (here the x-component). For the M-point of the second band we have plotted the field and phase along a polarisation direction rotated $60°$ with respect to the Cartesian coordinate system.

3. Group-velocity dispersion of Bloch modes

An important part of spatiotemporal control of waves in the PCF-type periodic structures is the fact that different Bloch modes propagating along the structure will experience different temporal dispersion. Thus selective excitation of Bloch modes provides an effective way for manipulation of the dispersion of an optical wave-packet. In this section we describe the contribution to the GVD from both the geometry and the materials the waveguides are made of. First we consider the contribution from the geometry, i.e. we analyze the dispersion of the modes when the wavelength dependence of the refractive indices is neglected. We focus on the dispersion of the modes at the edges of the first band (Γ- and K-point), and at the top of the second band, because they can be easily excited experimentally [26]

3.1. Geometrical dispersion

The dispersion of a given Bloch mode is defined in the following way

$$D = \frac{\omega^2}{2\pi c v_g^2} \frac{dv_g}{d\omega}, \tag{3}$$

where $v_g = (d\beta/d\omega)^{-1}$ is the group velocity. Here we calculate the group velocity as $v_g = \mathrm{Re}\langle \mathbf{E}^* \times \mathbf{H}, \mathbf{E}^* \times \mathbf{H}\rangle_z / \langle \mathbf{H}, \mathbf{H}\rangle$, which is exact when material dispersion is neglected (the notation $\langle \cdot, \cdot \rangle$ denotes the inner product). The values $D < 0$ correspond to *normal dispersion*, and $D > 0$ corresponds to *anomalous dispersion*. In Fig. 2 the normalized dispersion ($c\Lambda D$) of the Bloch modes corresponding to the top and bottom of the first band (Γ- and K-point respectively), and the top of the second band are plotted for three different index contrasts ($\Delta n = 10^{-3}$, $5 \cdot 10^{-2}$, and 10^{-1}). The index of the silica background is fixed at 1.44, and we consider a structure with $d/\Lambda = 0.5$. The wavelength at which the fundamental bandgap opens up, depends on the index contrast. For the index contrasts $\Delta n = 10^{-3}$, $5 \cdot 10^{-2}$, and 10^{-1}, the fundamental bandgap exists for $\lambda/\Lambda \leq 0.11$, 0.73, and 0.98, respectively. Additionally, in Fig. 2(a) we show the dispersion of the fundamental HE_{11} mode of an isolated waveguide in order to compare how the dispersion is significantly changed at long wavelengths in the periodic structure. Note that the dispersion in Fig. 2(a) is plotted as a function of $\lambda/(2d)$, in order to enable direct comparison with the dispersion for the periodic structure that has $d/\Lambda = 0.5$. At short wavelengths the dispersion of the HE_{11} mode of an isolated waveguide, and the modes corresponding to the top and bottom of the first band [Fig. 2(b,c)] are similar. This is also expected since these modes are highly
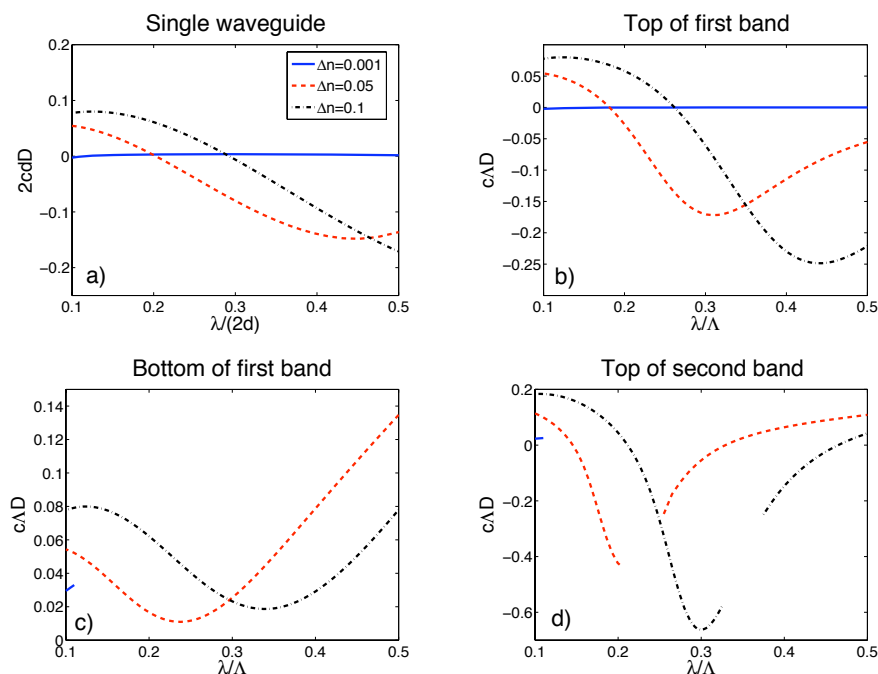
Fig. 2. (a) Normalized geometrical dispersion of the fundamental mode of an isolated waveguide. (b) and (c) show the normalized dispersion of the Bloch mode corresponding to the top and bottom of the first band respectively, and (d) shows the normalized dispersion of the mode at the top of the second band. $d/\Lambda = 0.5$ for (b), (c) and (d). Note that in (c) and (d) the dispersion is only shown when the fundamental bandgap exists.

confined inside the high-index inclusions at small wavelengths, and are therefore not affected by the periodic geometry. In Fig. 2(c) the dispersion of the modes lying at the bottom of the first band are shown. We see that for these modes large anomalous dispersion ($c\Lambda D > 0$) can be achieved for both small and high index contrasts. This anomalous dispersion makes these modes very attractive for temporal localisation of pulses, and we will explore their applicability for spatiotemporal localisation later on in the paper. Note that the dispersion is only shown when a bandgap exists ($\lambda/\Lambda < 0.1$) for $\Delta n = 10^{-3}$. In Fig. 2(d) the dispersion of the mode lying at the top of the second band is shown. We see that high anomalous dispersion can be achieved at small wavelengths compared to the pitch ($\lambda/\Lambda < 0.2$). The reason why there are discontinuities in the dispersion for $\Delta n = 0.05$ and 0.1 at $\lambda/\Lambda = 0.25$ and 0.35, respectively is that the mode bounding the top of the second band changes its character at that wavelength due to band crossing. Hence we cannot uniquely define the dispersion of the mode at the top of the second band when the two bands cross.

The regions of anomalous dispersion, which we identified above, are of special interest as they define a window of possible existence of bright temporal solitons in the array. When the PCF cladding is infiltrated with a liquid it is important to have a strong anomalous geometrical dispersion in order to compensate the normal chromatic dispersion of the material. We note that most liquids suitable for infiltration of PCFs have normal dispersion in the visible and near infrared spectrum. If the multi-core structure is all glass [34] it is possible to have anomalous material dispersion in the infrared spectrum. SiO_2 for example, has anomalous dispersion for wavelengths above 1.3 m, and anomalous chromatic dispersion in an all glass structure can

Table 1. Parameters for refractive index formulas given in Eqs. (4-5).

i	A_i	a_i	b_i
1	1.580826	0.6965325	$4.368309 \cdot 10^{-3}\,[\text{m}^2]$
2	$1.52389 \cdot 10^{-2}\,[\text{m}^2]$	0.4083099	$1.394999 \cdot 10^{-2}\,[\text{m}^2]$
3	$4.8578 \cdot 10^{-4}\,[\text{m}^4]$	0.8968766	$97.93399\,[\text{m}^2]$
4	$-8.2863 \cdot 10^{-5}\,[\text{m}^6]$	–	–
5	$1.4619 \cdot 10^{-5}\,[\text{m}^8]$	–	–
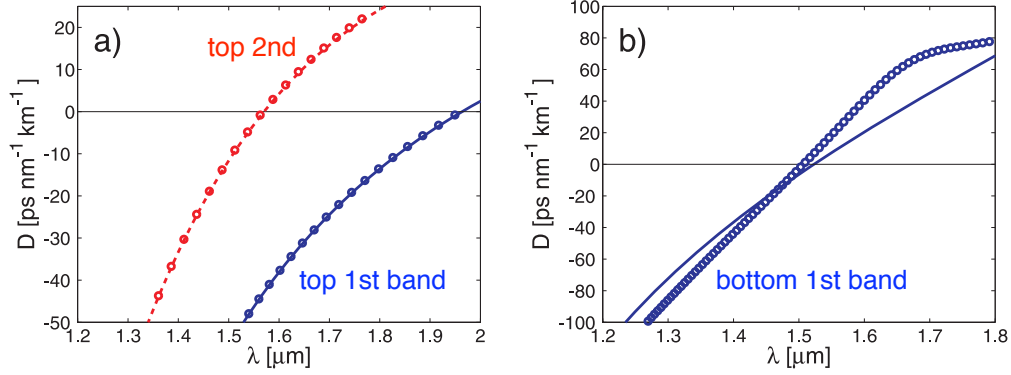
Fig. 3. (a) Chromatic dispersion of Bloch modes corresponding to the top of the first (solid blue line) and second band (dashed red line), and the dispersion of the corresponding defect modes (blue and red points) for $\Delta n_{NL} = 10^{-3}$. (b) Chromatic dispersion of Bloch mode corresponding to the bottom of first band (blue line), and the dispersion of the corresponding defect mode for $\Delta n_{NL} = -10^{-3}$ (blue points). The dimensions of the structures are (a) $d/\Lambda = 0.45, \Lambda = 10$ m, and (b) $d/\Lambda = 0.60, \Lambda = 3.5$ m.

therefore be obtained in this spectral region even with normal geometrical dispersion.

3.2. Chromatic dispersion

In this section we include the contribution of the material dispersion from both high index material and the surrounding silica matrix. We focus on the case where the array is infiltrated with CS_2, since this liquid has fast and strong third order nonlinearity. CS_2 also has good transmission in the visible and near infrared spectrum [37]. The refractive indices of silica and CS_2 are found with the following formulas:

$$n_{\text{SiO}_2}^2 = 1 + \sum_{j=1}^{3} \frac{a_j \lambda^2}{\lambda^2 - b_j}, \tag{4}$$

$$n_{\text{CS}_2} = A_1 + A_2 \lambda^{-2} + A_3 \lambda^{-4} + A_4 \lambda^{-6} + A_5 \lambda^{-8}, \tag{5}$$

The values of the parameters a_i and A_i, which are listed in Table 1, are taken from Refs. [38] and [36], respectively.

Using Eqs. (4)-(5) we find that the material dispersion of silica and CS_2 is $D_{\text{SiO}_2} = 22\,\text{ps/(nm·km)}$ and $D_{\text{CS}_2} = -85\,\text{ps/(nm·km)}$ at $\lambda_0 = 1.55$ m. We have solved Eq. (1) self consistently by including the wavelength dependent refractive index of the dielectric constant for both silica and CS_2. Here we propose two different designs that have anomalous dispersion for

the mode at the top of the second band and the mode at the bottom of the first band. In Fig. 3(a) the chromatic dispersion of the modes at the top of the first (blue line) and second (red line) bands is shown for a design with $d/\Lambda = 0.45$ and $\Lambda = 10$ μm corresponding to the parameters of a commercially available LMA-25 fibre (Crystal Fibre A/S, Denmark). The mode at the bottom of the first band [not shown in Fig. 3(a)] experiences almost identical dispersion as the mode at the top of the first band. This is also expected since the pitch is much larger than the wavelength, and therefore the bands are very flat in this region. For the design consisting of a triangular silica matrix infiltrated with CS_2, we have varied the pitch and the relative hole diameter, and found that for the case of Bloch waves at the top of the first band it is not possible to achieve anomalous dispersion in the range of $1.2 - 1.8$ μm. This is a consequence of the strong normal dispersion of the CS_2, which can not be compensated by the weak geometrical anomalous dispersion of the array. For the higher order mode (top of second band) much stronger geometrical anomalous dispersion can be obtained, and anomalous dispersion can be achieved. For the example shown in Fig. 3(a) we find a zero dispersion wavelength (ZDW) of $\lambda_{ZDW} = 1.57$ μm, and an anomalous dispersion of 4 ps/(nm·km) at $\lambda = 1.6$ μm.

If we instead consider a different design with $d/\Lambda = 0.60$ and $\Lambda = 3.5$ μm we can obtain much higher anomalous dispersion of the bottom of the first band, as suggested by the plot of the waveguide dispersion of this mode shown in Fig. 2(c). In Fig. 3(b) the dispersion for a CS_2 infiltrated array with $d/\Lambda = 0.60$ and $\Lambda = 3.5$ μm is shown. Here $\lambda_{ZDW} = 1.51$ μm, and the dispersion at $\lambda = 1.60$ μm is 20 ps/(nm·km). While in this case anomalous dispersion can be achieved for the bottom of the first band, the dispersion of the top of the first and second bands [not shown in Fig. 3(b)] lies deep into the normal regime. From this investigation of the chromatic dispersion of the Bloch modes, we conclude that for the specific case we are considering, it is necessary to use either the top of the second band, or the bottom of the first band in order to achieve anomalous dispersion.

4. Soliton defect modes

In the previous section we showed that anomalous dispersion is possible only in regions where the geometrical part of the dispersion is strongly anomalous, because of the normal dispersion of the liquid throughout the visible and near infrared spectrum. Only in these regions a self-focusing positive nonlinearity can balance the dispersion effect. However, for formation of STSs the same focusing nonlinearity has to be able to balance the beam diffraction, which is also dramatically changed due to periodicity. Beams experiencing *normal* (positive) *diffraction* correspond to the top of each band, while beams associated with Bloch waves from the bottom of the bands experience *anomalous* (negative) *diffraction*. Therefore, pure STS can only exist when the beam is associated with the top of the first or second band for wavelengths $\lambda > 1.95$ μm and $\lambda > 1.57$ μm, respectively [see Fig. 3(a)].

CS_2 for example, has a strong focusing nonlinearity of the order of $n_2 \approx 0.75 \cdot 10^{-18} \text{m}^2/\text{W}$ in the wavelength range $800 - 1600$ nm for 100 fs pulses [39]. Hence we can induce a positive defect in the array, by injecting a high intensity pulse in one of the waveguides. The maximal induced defect can be approximated as $\Delta n_{NL} \approx P_0 n_2/(\pi r^2)$, where P_0 is the peak power of the laser pulses, and r is the hole radius. If the holes have a radius of 2.25 μm, we can induce a defect of $\Delta n_{NL} = 10^{-3}$ with a pulse with a peak power of $P_0 = 21.2$ kW, which is typical for a femtosecond fiber laser at a wavelength of 1.5 μm .

On the other hand, wave-packets associated with the bottom of the first band show the strongest anomalous dispersion [Fig. 3(b)]. As mentioned above, these wave-packets however, exhibit anomalous diffraction which can not be balanced by the focusing nonlinearity. In order to employ such beams as STSs one needs to use *hybrid scheme* for localization. In this scheme two different types of nonlinearity need to be employed for compensation of pulse
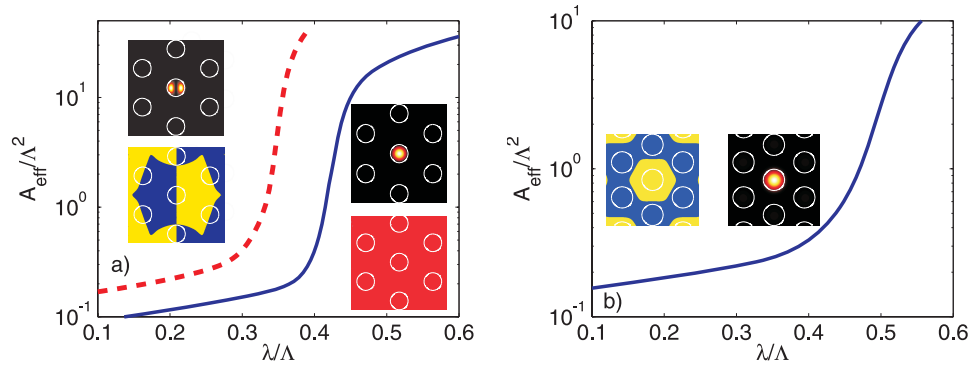
Fig. 4. Normalized effective area for defect mode in a 2D hexagonal structure. The index the silica background has been set to 1.44, and the index in the holes is 1.59. (a) $d/\Lambda = 0.45$ and defect $\Delta n = +10^{-3}$. The solid line shows the results for the defect mode in the semi-infinite bandgap above the first band, and the dotted line shows the results for the defect mode in the fundamental bandgap just above the edge of the second band. Insets: Intensities and phases of the defect modes at $\lambda/\Lambda = 0.15$. (b) $d/\Lambda = 0.60$ and defect $\Delta n = -10^{-3}$. The insets show the intensity and phase of the defect mode at $\lambda/\Lambda = 0.43$.

dispersion and beam diffraction, respectively. A defocusing type of nonlinearity such as slow thermal nonlinearity of the liquid can be employed for spatial localization, while a self-focusing fast electronic response can be responsible for temporal localization. We note that in this case the fast nonlinearity should be weaker than the defocusing, so the total induced defect will always remain negative. A negative defect can be induced by a thermooptic effect, which arises when a small portion of the light is absorbed and heats the liquid. Since CS_2 has a relatively large thermooptic coefficient of $dn/dT = -7.9 \cdot 10^{-4} K^{-1}$ [37], index changes of the order of 10^{-3} could be achieved even at small absorption levels. In this case the negative defect strength will depend not on the peak pulse power, but on the average beam power. Thus there will be two control parameters, which will contribute to the spatiotemporal localization: pulse peak power and average beam power. Further challenges associated with this scheme, including the spatially nonlocal aspect of thermal nonlinearity needs to be investigated.

The spatial localization of the wave-packet due to nonlinear material response can be regarded as the formation of nonlinear defect modes. In the case of strong nonlinear localization, when the mode is confined to a single waveguide of the periodic structure, one can take a quasi-linear approach for their theoretical treatment. With this approach we consider the localized gap modes that exist when the periodicity of the crystal is broken, by raising or lowering the refractive index of one of the infiltrated holes. If the index of one of the holes is slightly increased, localized modes exist with propagation constants inside the bandgaps of the perfect structure. These modes will have propagation constants bifurcating from the top of the bands, i.e. defect modes in the fundamental bandgap will bifurcate from the top of the second band. If the induced defect is negative, the defect modes will bifurcate from the bottom of the bands bounding the top of the gaps.

An important task, however, is to understand how such spatial localization changes its temporal dispersion in comparison to the dispersion of the corresponding Bloch mode. Intuitively, if the propagation constant of the localized mode remains close to the band-edge its dispersion should be only weakly affected by the localization. This fact, however requires a detailed analysis which is presented in this section.

To analyze the defect modes we use linear theory and solve Eq. (1) for a dielectric function

$\varepsilon(\mathbf{r})$, which is not periodic. This is done using a full-vectorial commercial finite element mode solver [40]. In the simulated structure we use 6 rings of holes around the hole with the non-linearity induced defect. The main part of the energy of a defect mode is localised inside the defect if the wavelength is sufficiently small. In Fig. 4 we plot the normalized effective area $(A_{eff} = \langle \mathbf{E}, \mathbf{E} \rangle^2 / \langle |\mathbf{E}|^2, |\mathbf{E}|^2 \rangle)$ of the defect modes as a function of normalized wavelength for defects of $\Delta n = \pm 10^{-3}$. In Fig. 4(a) we show the results for a positive defect, which allows defect modes in the semi-infinite bandgap above the first band (solid line), and in the fundamental bandgap (dashed line). The structure has $d/\Lambda = 0.45$ such that anomalous dispersion can be achieved for the mode at the top of the second band at 1.6 m [see Fig. 3(a)]. We see that for an induced index change of only $\Delta n = 10^{-3}$, the defect mode existing in the semi-infinite gap becomes strongly localized on the defect for $\lambda/\Lambda < 0.4$, while the defect mode in the fundamental bandgap becomes localized when $\lambda/\Lambda < 0.35$.

Using the result for the structure presented in Fig. 3(a), which also has $d/\Lambda = 0.45$, we see that $\lambda/\Lambda > 0.16$ is necessary in order to achieve anomalous dispersion. Therefore such conditions allow for simultaneous spatial localization and anomalous dispersion.

In Fig. 4(b) the results for the defect mode existing in the fundamental bandgap for a negative defect of $\Delta n = -10^{-3}$ are shown. The structure has $d/\Lambda = 0.60$, and we see that the defect mode becomes localized when $\lambda/\Lambda < 0.5$. Using the result for the structure presented in Fig. 3(b), which also has $d/\Lambda = 0.60$, we see that $\lambda/\Lambda > 0.43$ is necessary in order to achieve anomalous dispersion. Therefore, in this case it is also possible to have an array where spatial localization and anomalous dispersion appear simultaneously.

To demonstrate that the dispersion of the extended Bloch modes at the band-edges calculated in the previous section really are a good approximation to the dispersion of the defect modes, we have included in Fig. 3 the dispersion of the defect modes (shown with points) together with their corresponding Bloch mode (lines). We see that the dispersion of the defect modes indeed follows the dispersion of their associated Bloch modes. This is also a great advantage from a computational point of view, since the calculation of the modes of the perfect structure is usually much faster than the calculation of the dispersion of the defect modes.

To summarize the results of this section, we have found specific designs based on CS_2 infiltrated arrays, that allows for simultaneous spatial localization and anomalous dispersion. In the following section we discuss the criteria that should be satisfied in order to use the anomalous dispersion for temporal localization.

5. Spatiotemporal localization

In the previous sections we described the conditions when anomalous dispersion and normal diffraction appear simultaneously, which identify the range for possible existence of STS. An important additional condition however, is to obtain similar or equal values for the lengths of dispersion and diffraction in the fibre. These characteristics are dependent on the initial excitation conditions (beam and pulse width) and here we aim to identify the practically feasible cases. In particular, we are interested in strongly spatially-localized solutions, which are close to the defect modes presented in the previous section. We would also like to point out that the use of short (and ultra-short) pulses is well accommodated in our analysis as the nonlinearity of the materials is not resonant [39] and special phase-matching methods [11,12] are not required.

5.1. Coupling length

In the following we analyze the diffraction of the Bloch modes. Using standard coupled mode theory, the linear propagation in the first band of a hexagonal lattice is governed by the coupled
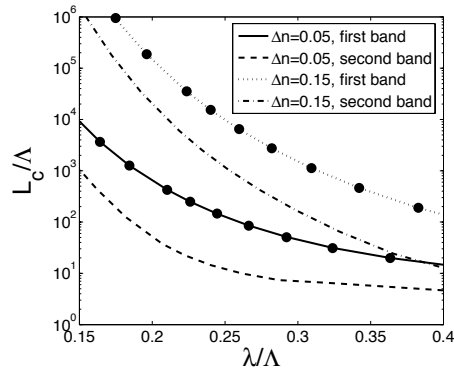
Fig. 5. Coupling length for different index contrasts for a structure with $d/\Lambda = 0.5$. The refractive index of the background is fixed at 1.44, corresponding to silica at $\lambda_0 = 1.5$ m. The black dots show the result of the coupled mode approximation for the first band.

equations [41]

$$i\frac{dA_{mn}}{dz} + C(A_{m+1,n} + A_{m,n+1} + A_{m-1,n+1} + A_{m-1,n} + A_{m,n-1} + A_{m+1,n-1}) = 0, \tag{6}$$

where A_{mn} is the amplitude at the lattice point (m,n), and C is the coupling constant. Inserting the Bloch wave ansatz $A_{mn} = A_0 \exp(i[\mathbf{r}_\perp \cdot \mathbf{k}_\perp + \beta z])$ we find the dispersion relation

$$\beta = 2C\left\{\cos[2\pi k_1] + \cos[2\pi k_2] + \cos[2\pi(k_1 - k_2)]\right\}, \tag{7}$$

where (k_1, k_2) are the coordinates of the considered k-point in reciprocal space in the basis of the reciprocal lattice vectors. We define the coupling length as the minimum longitudinal distance a mode must propagate before its center moves by one lattice period in the transversal plane. Since the propagation direction of a mode is given by the normal to the diffraction surface defined by $\beta(k_x, k_y)$, the coupling length is given by

$$L_c = \frac{\Lambda}{\max_{k_x,k_y} |\nabla_{k_x,k_y}\beta|}. \tag{8}$$

Using the approximate diffraction relation in Eq. (7) we find that for the first band $L_c = 2.56/\Delta\beta$, where $\Delta\beta$ is the difference between the smallest and the largest propagation constants at fixed frequency in the first band.

In the second band we calculate the coupling length directly from Eq. (8), using a diffraction relation found numerically. In Fig. 5 the coupling length is plotted for the first and second bands in an array with $d/\Lambda = 0.5$ and background index of $n = 1.44$. The coupling length is shown for two different index contrasts, $\Delta n = 0.05$ and $\Delta n = 0.15$, the latter corresponding to silica and CS_2. We see that the coupling length increases with decreasing wavelength, since the modes become more localized inside the high-index regions at shorter wavelengths, and only weakly overlap with the fields in the neighboring waveguides. The same happens when the index contrast is increased. The coupling length for the mode corresponding to the second band is about one order of magnitude shorter than in the first band. From an experimental point of view it will therefore be advantageous to use the second band, since this will require shorter infiltration lengths.

5.2. Dispersion length

In order to specify the requirements for the temporal localization we use well-known theory from nonlinear pulse propagation in optical fibers [3]. The nonlinear coefficient is defined as $\gamma = 2n_2\pi/(\lambda A_{eff})$, where A_{eff} is the effective area of the given mode. The nonlinear length is then given by $L_{NL} = 1/(P_0\gamma)$. This is the propagation length required to achieve a phase shift of 1 in the center of the pulse, when only nonlinear effects are present. The dispersion length is given by $L_D = T_0^2/|\beta_2|$, where $\beta_2 = d^2\beta/d\omega^2$. This is the length a Gaussian pulse must propagate in order to broaden its temporal width by a factor of $\sqrt{2}$ in the presence of only linear effects. The soliton number is then defined as $N = \sqrt{L_D/L_{NL}}$. If we assume that the propagation can be described using a standard nonlinear Schrödinger equation that only takes second order dispersion and an instantaneous Kerr response into account, it can be shown that we have a periodic soliton solution whenever the soliton number is an integer. However, it is only possible to demonstrate temporal localization experimentally if the soliton number is small, preferably equal to 1.

5.3. Localization in space and time

The design presented here with a focusing nonlinearity (positive defect) [Figs. 3(a) and 4(a)] has a soliton number much larger than 1, since a high peak power will be required to make the spatial localization (20 kW). Making the soliton number equal to 1 with such a high peak power, and the dispersion shown in Fig. 3(a), would then require a pulse with full width half maximum of less than 10 fs, which is not feasible experimentally, because of the non-instantaneous nature of the nonlinear response of CS_2 [39], and the large spectral bandwidth of the pulses. Another problem with the design suggested in Fig. 3(a) ($\lambda/\Lambda \sim 0.15$) is that the coupling length would be in the order of meters as shown in Fig. 5, therefore it would be required to infiltrate a very long piece of fiber with CS_2 to demonstrate the spatial localization.

   A way to overcome these problems could be to use the idea of hybrid nonlinearity discussed in Section 4, where the self-defocusing thermal nonlinear response of CS_2 is used to create a negative defect for spatial localization, while the self-focusing Kerr nonlinearity is responsible for temporal pulse confinement. Using the design presented in Fig. 3(b) ($\lambda/\Lambda \sim 0.4$) we find that a pulse with a peak power of only 60 W is sufficient to create a fundamental soliton ($N = 1$), if the temporal width is chosen to be $T_{FWHM} = 100$ fs ($T_{FWHM} = 1.763 \cdot T_0$, i.e. we assume a sech-shaped pulse) and the wavelength is 1.6 m, where the GVD of the defect mode is 40 ps/(nm·km). The coupling length for this design would be of the order of one millimeter, and $L_D = L_{NL} \approx 5$ cm, hence a 10 cm fiber would be enough to demonstrate both the spatial and temporal localization. The induced index change will then depend on the pulse repetition rate and the light absorption in the liquid, but because of the moderate peak power, the nonlinear index change due to the Kerr effect will be much weaker. The pulse repetition rate and the light absorption can both be controlled independently in experiments. The absorption could for example be adjusted by adding a dye to the liquid before infiltration.

6. Conclusions

We have presented a novel practically realistic platform for observation of spatiotemporal solitons (or light bullets) in liquid infiltrated hexagonal waveguide arrays. We have analyzed the group-velocity dispersion of Bloch modes with a special focus on arrays infiltrated with CS_2. It is shown that defect modes with anomalous group velocity dispersion exist in the fundamental bandgap of the structure for both positive and negative induced defects depending on the structure of the array. We have examined the possibilities for realizing light bullets in such structures, and shown that the most experimentally feasible scheme of spatiotemporal localization should

involve the fundamental bandgap with a negative induced defect. This can be realized by using a hybrid type of nonlinearity, where a slow defocusing nonlinearity is employed for spatial localization, while fast and weaker positive nonlinearity is responsible for temporal localization.

Acknowledgments